Supplemental Material for
Inverse design of few-layer metasurfaces empowered by the matrix theory of multilayer optics

Zhancheng Li,[1] Wenwei Liu,[1] Dina Ma,[1] Shiwang Yu,[1] Hua Cheng,[1, *] Duk-Yong Choi,[2] Jianguo Tian,[1] and Shuqi Chen[1, 3, 4, †]

[1] *The Key Laboratory of Weak Light Nonlinear Photonics,*
Ministry of Education, Renewable Energy Conversion and Storage Center,
School of Physics and TEDA Institute of Applied Physics, Nankai University, Tianjin 300071, China
[2] *Laser Physics Centre, Research School of Physics and Engineering,*
Australian National University, Canberra, ACT 2601, Australia
[3] *The Collaborative Innovation Center of Extreme Optics,*
Shanxi University, Taiyuan, Shanxi 030006, China
[4] *Collaborative Innovation Center of Light Manipulations and Applications,*
Shandong Normal University, Jinan 250358, China
(Dated: January 15, 2022)

I. THE MATRIX THEORY OF MULTILAYER OPTICS

The scattering characteristics of metasurfaces to electromagnetic waves can be described by their scattering matrix S.[1, 2] By involving the transmission and reflection coefficients in both the forward and backward directions, the scattering waves from a planar medium can be expressed in terms of the incident waves, as show in Figure S1(a):

$$
\begin{bmatrix} \mathbf{E}_{\text{out}}^{f} \\ \mathbf{E}_{\text{out}}^{b} \end{bmatrix} = \mathbf{S} \begin{bmatrix} \mathbf{E}_{\text{in}}^{f} \\ \mathbf{E}_{\text{in}}^{b} \end{bmatrix} = \begin{bmatrix} \mathbf{t}^{f} & \mathbf{r}^{b} \\ \mathbf{r}^{f} & \mathbf{t}^{b} \end{bmatrix} \begin{bmatrix} \mathbf{E}_{\text{in}}^{f} \\ \mathbf{E}_{\text{in}}^{b} \end{bmatrix} ,
\tag{S1}
$$

in which $\mathbf{t}^{f}$ and $\mathbf{r}^{f}$ are the matrices of the transmission and reflection coefficients in the forward direction, while $\mathbf{t}^{b}$ and $\mathbf{r}^{b}$ are the matrices of the transmission and reflection coefficients in the backward direction. More specifically, considering that the basis polarization vectors of the incident and outgoing fields are linear-polarized vectors in the x and y directions, we can further express Equation S1 as,

$$
\begin{bmatrix} E_{\text{out}}^{f,x} \\ E_{\text{out}}^{f,y} \\ E_{\text{out}}^{b,x} \\ E_{\text{out}}^{b,y} \end{bmatrix} = \mathbf{S} \begin{bmatrix} E_{\text{in}}^{f,x} \\ E_{\text{in}}^{f,y} \\ E_{\text{in}}^{b,x} \\ E_{\text{in}}^{b,y} \end{bmatrix} = \begin{bmatrix} t_{xx}^{f} & t_{xy}^{f} & r_{xx}^{b} & r_{xy}^{b} \\ t_{yx}^{f} & t_{yy}^{f} & r_{yx}^{b} & r_{yy}^{b} \\ r_{xx}^{f} & r_{xy}^{f} & t_{xx}^{b} & t_{xy}^{b} \\ r_{yx}^{f} & r_{yy}^{f} & t_{yx}^{b} & t_{yy}^{b} \end{bmatrix} \begin{bmatrix} E_{\text{in}}^{f,x} \\ E_{\text{in}}^{f,y} \\ E_{\text{in}}^{b,x} \\ E_{\text{in}}^{b,y} \end{bmatrix} .
\tag{S2}
$$

For a planar layered medium, the outgoing waves can also be expressed in terms of the incident waves by utilizing the wave-transfer matrix $\mathbf{M}$, as shown in Figure S1(b):

$$
\begin{bmatrix} \mathbf{E}_{\text{out}}^{f} \\ \mathbf{E}_{\text{in}}^{b} \end{bmatrix} = \mathbf{M} \begin{bmatrix} \mathbf{E}_{\text{in}}^{f} \\ \mathbf{E}_{\text{out}}^{b} \end{bmatrix} = \begin{bmatrix} \mathbf{m}_{\text{a}} & \mathbf{m}_{\text{b}} \\ \mathbf{m}_{\text{c}} & \mathbf{m}_{\text{d}} \end{bmatrix} \begin{bmatrix} \mathbf{E}_{\text{in}}^{f} \\ \mathbf{E}_{\text{out}}^{b} \end{bmatrix} .
\tag{S3}
$$

Moreover, Equation S3 can also be further expressed as

$$
\begin{bmatrix} E_{\text{out}}^{f,x} \\ E_{\text{out}}^{f,y} \\ E_{\text{in}}^{b,x} \\ E_{\text{in}}^{b,y} \end{bmatrix} = \mathbf{M} \begin{bmatrix} E_{\text{in}}^{f,x} \\ E_{\text{in}}^{f,y} \\ E_{\text{out}}^{b,x} \\ E_{\text{out}}^{b,y} \end{bmatrix} = \begin{bmatrix} m_{\text{a}1} & m_{\text{a}2} & m_{\text{b}1} & m_{\text{b}2} \\ m_{\text{a}3} & m_{\text{a}4} & m_{\text{b}3} & m_{\text{b}4} \\ m_{\text{c}1} & m_{\text{c}2} & m_{\text{d}1} & m_{\text{d}2} \\ m_{\text{c}3} & m_{\text{c}4} & m_{\text{d}3} & m_{\text{d}4} \end{bmatrix} \begin{bmatrix} E_{\text{in}}^{f,x} \\ E_{\text{in}}^{f,y} \\ E_{\text{out}}^{b,x} \\ E_{\text{out}}^{b,y} \end{bmatrix} .
\tag{S4}
$$

For a multilayered medium, the overall wave-transfer matrix $\mathbf{M}_{\text{all}}$ can be treated as the product of the wave-transfer matrix of each layer, as shown in Figure S1(c):

$$
\mathbf{M}_{\text{all}} = \mathbf{M}_{\text{N}} \cdots \mathbf{M}_{2} \mathbf{M}_{1} .
\tag{S5}
$$

Equation S5 is the wave-transfer matrix cascade formula. When the near-field interactions between the layers in a few-layer metasurface are negligible, the wave-transfer matrix method associated with Equation S5 can be used to describe the scattering characteristics of the few-layer metasurface based on the scattering properties of each layer. We take a few-layer metasurface (shown in Figure S1(d)) as an example. For a planar interface between two media i and j (whether with or without nanostructures), the forward and backward propagating waves can be related by utilizing a 4×4 wave-transfer Matrix $\mathbf{M}_{ji}$, which can be expressed in terms of the reflection and transmission coefficients of the scattering matrix $\mathbf{S}$:

$$
\mathbf{M}_{ji} = \begin{bmatrix} 1 & 0 & -r_{xx}^{b} & -r_{xy}^{b} \\ 0 & 1 & -r_{yx}^{b} & -r_{yy}^{b} \\ 0 & 0 & t_{xx}^{b} & t_{xy}^{b} \\ 0 & 0 & t_{yx}^{b} & t_{yy}^{b} \end{bmatrix}^{-1} \begin{bmatrix} t_{xx}^{f} & t_{xy}^{f} & 0 & 0 \\ t_{yx}^{f} & t_{yy}^{f} & 0 & 0 \\ -r_{xx}^{f} & -r_{xy}^{f} & 1 & 0 \\ -r_{yx}^{f} & -r_{yy}^{f} & 0 & 1 \end{bmatrix} .
\tag{S6}
$$
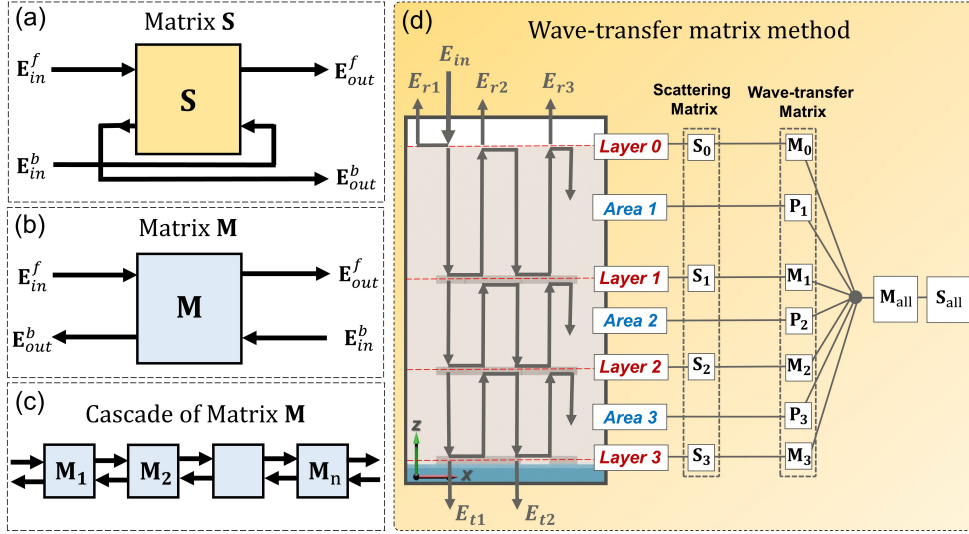
Moreover, $\mathbf{M}_{ji}$ can be further expressed as:

FIG. S1. Illustrating of the matrix theory of multilayer optics. Schematic diagram of (a) the scattering matrix $\mathbf{S}$, (b) the wave-transfer matrix $\mathbf{M}$, and (c) the cascade of matrix $\mathbf{M}$. (d) Illustrating of the wave-transfer matrix method for the calculation of the electromagnetic characteristics of few-layer metasurfaces. A metasurface containing three layers of metallic artificial nanostructures embedded in a dielectric substrate is taken as an example.

$$
\begin{aligned}
\mathbf{M}_{ji} &= \begin{bmatrix} \mathbf{I} & -\mathbf{r}^b \\ 0 & \mathbf{t}^b \end{bmatrix}^{-1} \begin{bmatrix} \mathbf{t}^f & 0 \\ -\mathbf{r}^f & \mathbf{I} \end{bmatrix} \\
&= \begin{bmatrix} \mathbf{I} & \mathbf{r}^b(\mathbf{t}^b)^{-1} \\ 0 & (\mathbf{t}^b)^{-1} \end{bmatrix} \begin{bmatrix} \mathbf{t}^f & 0 \\ -\mathbf{r}^f & \mathbf{I} \end{bmatrix} \\
&= \begin{bmatrix} \mathbf{t}^f - \mathbf{r}^b(\mathbf{t}^b)^{-1}\mathbf{r}^f & \mathbf{r}^b(\mathbf{t}^b)^{-1} \\ -(\mathbf{t}^b)^{-1}\mathbf{r}^f & (\mathbf{t}^b)^{-1} \end{bmatrix}
\end{aligned}
. \tag{S7}
$$

On the other hand, the wave transfer matrix $\mathbf{P}_i$ of a homogeneous medium i (thickness equals d and refractive index is n) is:

$$
\mathbf{P}_i = \begin{bmatrix} e^{-ik_0 nd} & 0 & 0 & 0 \\ 0 & e^{-ik_0 nd} & 0 & 0 \\ 0 & 0 & e^{ik_0 nd} & 0 \\ 0 & 0 & 0 & e^{ik_0 nd} \end{bmatrix}, \tag{S8}
$$

where k_0 is the free-space wave number. By utilizing the wave-transfer matrix cascade formula, the overall wave-transfer matrix $\mathbf{M}_{\mathrm{all}}$ of the proposed few-layer metasurface can be treated as:

$$
\mathbf{M}_{\mathrm{all}} = \mathbf{M}_3 \mathbf{P}_3 \mathbf{M}_2 \mathbf{P}_2 \mathbf{M}_1 \mathbf{P}_1 \mathbf{M}_0 , \tag{S9}
$$

Thus, the electromagnetic characstics of few-layer metasurfaces can be predicted based on the scattering matrix of each layer. If we know the scattering matrix $\mathbf{S}_{ji}$ of each layer, then we can calculate the corresponding wave-transfer matrix $\mathbf{M}_{ji}$. The overall wave-transfer matrix $\mathbf{M}_{\mathrm{all}}$ of the few-layer metasurface can be obtained by using the wave-transfer matrix cascade formula. Finally, the overall scattering matrix $\mathbf{S}_{\mathrm{all}}$ can be calculated based on:

$$
\mathbf{S} = \begin{bmatrix} \mathbf{m}_a - \mathbf{m}_b(\mathbf{m}_d)^{-1}\mathbf{m}_c & \mathbf{m}_b(\mathbf{m}_d)^{-1} \\ -(\mathbf{m}_d)^{-1}\mathbf{m}_c & (\mathbf{m}_d)^{-1} \end{bmatrix}. \tag{S10}
$$

II. DATA COLLECTION FOR THE TRAINING OF THE CNN SIMULATOR

The proof-of-concept metasurfaces designed on SiO_2 substrates are composed of multiple layers of aluminum nanostructures embedded into the SU-8 polymer. A data set containing the structural configurations and the corresponding scattering matrices of different planar aluminum nanostructures was built for the training of the convolutional neural network (CNN) simulator. In the designed metasurfaces, the periods of a unit cell in both the x and y directions are 450 nm. As shown in Figure S2(a), the planar aluminum nanostructures consist of several aluminum cuboids in which width $w = 70$ nm and thickness $t = 30$ nm. Every planar aluminum nanostructure is corresponding to a randomly generated 5×5 matrix in which the elements are equal to either 0 or 1. When the element of the matrix equals 1, an aluminum cuboid is built in the corresponding place. Otherwise, no aluminum cuboid is built. The scattering matrices of the planar aluminum nanostructures are obtained by utilizing the commercial software CST Microwave Studio (MWS). In our simulations, the unit cell boundary conditions were set in the x and y directions representing a periodical structure, and an open (perfectly matching layer) boundary was defined in the z direction for the light incidence and transmission while the excitation source was either a x- or a y-polarized plane wave.The permittivity of the SiO_2 and the SU-8 polymer were taken as 2.25, and the optical constants of aluminum were taken from Paliks handbook.[3] The simulation model is shown in Figure S2(b), the aluminum nanostructures is embedded in the middle of a SU-8 polymer with d = 2000 nm. The scattering matrix of the whole model under the normal incidence can be expressed as:

$$\begin{bmatrix} E_{\text{out}}^{2,x} \\ E_{\text{out}}^{2,y} \\ E_{\text{out}}^{1,x} \\ E_{\text{out}}^{1,y} \end{bmatrix} = \mathbf{S'} \begin{bmatrix} E_{\text{in}}^{1,x} \\ E_{\text{in}}^{1,y} \\ E_{\text{in}}^{2,x} \\ E_{\text{in}}^{2,y} \end{bmatrix} = \begin{bmatrix} t_{xx}^{21} & t_{xy}^{21} & r_{xx}^{22} & r_{xy}^{22} \\ t_{yx}^{21} & t_{yy}^{21} & r_{yx}^{22} & r_{yy}^{22} \\ r_{xx}^{11} & r_{xy}^{11} & t_{xx}^{12} & t_{xy}^{12} \\ r_{yx}^{11} & r_{yy}^{11} & t_{yx}^{12} & t_{yy}^{12} \end{bmatrix} \begin{bmatrix} E_{\text{in}}^{1,x} \\ E_{\text{in}}^{1,y} \\ E_{\text{in}}^{2,x} \\ E_{\text{in}}^{2,y} \end{bmatrix}, \tag{S11}$$

whose elements can be directly obtained from the simulation. According to the wave-transfer matrix method and Equation S10, the scattering matrix of the aluminum nanostructure is:

$$\begin{bmatrix} E_{\text{out}}^{f,x} \\ E_{\text{out}}^{f,y} \\ E_{\text{out}}^{b,x} \\ E_{\text{out}}^{b,y} \end{bmatrix} = \mathbf{S} \begin{bmatrix} E_{\text{in}}^{f,x} \\ E_{\text{in}}^{f,y} \\ E_{\text{in}}^{b,x} \\ E_{\text{in}}^{b,y} \end{bmatrix} = \begin{bmatrix} t_{xx}^{f} & t_{xy}^{f} & r_{xx}^{b} & r_{xy}^{b} \\ t_{yx}^{f} & t_{yy}^{f} & r_{yx}^{b} & r_{yy}^{b} \\ r_{xx}^{f} & r_{xy}^{f} & t_{xx}^{b} & t_{xy}^{b} \\ r_{yx}^{f} & r_{yy}^{f} & t_{yx}^{b} & t_{yy}^{b} \end{bmatrix} \begin{bmatrix} E_{\text{in}}^{f,x} \\ E_{\text{in}}^{f,y} \\ E_{\text{in}}^{b,x} \\ E_{\text{in}}^{b,y} \end{bmatrix}$$
$$= e^{i2k_0 nd} \begin{bmatrix} t_{xx}^{21} & t_{xy}^{21} & r_{xx}^{22} & r_{xy}^{22} \\ t_{yx}^{21} & t_{yy}^{21} & r_{yx}^{22} & r_{yy}^{22} \\ r_{xx}^{11} & r_{xy}^{11} & t_{xx}^{12} & t_{xy}^{12} \\ r_{yx}^{11} & r_{yy}^{11} & t_{yx}^{12} & t_{yy}^{12} \end{bmatrix} \begin{bmatrix} E_{\text{in}}^{f,x} \\ E_{\text{in}}^{f,y} \\ E_{\text{in}}^{b,x} \\ E_{\text{in}}^{b,y} \end{bmatrix}. \tag{S12}$$

Then, every element of the scattering matrix of the designed aluminum nanostructure can be obtained based on the corresponding element of the whole model, for example, $t_{xx}^{f} = t_{xx}^{21} e^{i2k_0 nd}$. From the simulation, we can obtain the real and the imaginary parts of each element in Equation S11, then the corresponding element for aluminum nanostructure was calculated by:

$$\text{Re}(t_{ji}^{k}) = Re(t_{ji}^{ml})cos\varphi - \text{Im}(t_{ji}^{ml})sin\varphi,$$
$$\text{Im}(t_{ji}^{k}) = Re(t_{ji}^{ml})sin\varphi + \text{Im}(t_{ji}^{ml})\cos\varphi. \tag{S13}$$

where $\varphi=2k_0 nd$, Re and Im represent the real and imaginary part of a complex number. The subscript "i" and "j" indicate "x" or "y" while the superscript "k" indicates "f" or "b". The superscript "l" and "m" indicate "1" or "2".

In every simulation, two matrices are stored. The 5×5 matrix (Feature) whose elements equal 1 or 0 represents the structure configuration of the designed aluminum nanostructure. The 32×151 matrix (Label) contains the real and the imaginary parts of every element of the scattering matrix of the designed aluminum nanostructure at 151 different frequencies. We collected 23000 samples with the numerical simulation.

When the planar aluminum nanostructure rotates 90 degrees along the axis perpendicular to its surface, its scattering matrix can be expressed as:
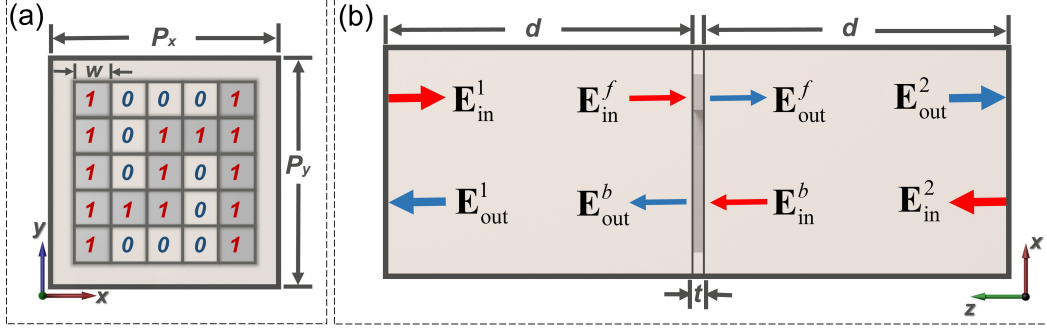
FIG. S2. Data set collection for the training of the CNN simulator. (a) Schematic of a designed planar aluminum nanostructure. (b) illustrating of the theoretical model for the calculation of the scattering matrix $\mathbf{S}$ of the designed planar aluminum nanostructure.

$$\mathbf{S'}=\begin{bmatrix} t_{yy}^f & -t_{yx}^f & r_{yy}^b & -r_{yx}^b \\ -t_{xy}^f & t_{xx}^f & -r_{xy}^b & r_{xx}^b \\ r_{yy}^f & -r_{yx}^f & t_{yy}^b & -t_{yx}^b \\ -r_{xy}^f & r_{xx}^f & -t_{xy}^b & t_{xx}^b \end{bmatrix}. \tag{S14}$$

This means that we could have twice the number of samples (46000) by rotating the aluminum nanostructure 90 degrees along the z-axis. Owing to that the planar aluminum nanostructure is mirror-symmetric with respect to the x-y plane, its scattering matrix can be further expressed as:[2]

$$\mathbf{S}=\begin{bmatrix} t_{xx}^f & t_{xy}^f & r_{xx}^f & r_{xy}^f \\ t_{yx}^f & t_{yy}^f & r_{yx}^f & r_{yy}^f \\ r_{xx}^f & r_{xy}^f & t_{xx}^f & t_{xy}^f \\ r_{yx}^f & r_{yy}^f & t_{yx}^f & t_{yy}^f \end{bmatrix}. \tag{S15}$$

Thus, the 32×151 matrix associated with the scattering matrix of the aluminum nanostructure can be represent by a 16×151 matrix. Finally, the label for the training of the CNN simulator has a dimension of 2416 (16×151). It needs to be pointed out that the structural mirror symmetry of the planar aluminum nanostructure also results in some other relationships between the coefficients of its scattering matrix (for example, the cross-polarized coefficients t_{xy}^f and t_{yx}^f are equivalent), but we did not consider these relationships any further. Meanwhile, we changed the elements of the 5×5 matrix, which equal to 0, into -1 to avoid the zero value and obtain the final feature matrix consisting of 1 and -1.

III. ARCHITECTURE OF THE CNN SIMULATOR AND THE TRAINING DETAILS

We trained a CNN simulator to efficiently predict the scattering matrices of the monolayer metasurfaces. Figure S3 is an illustration of the architecture of the CNN simulator. The CNN simulator was trained by using the 40000 collected simulation data, while another 3000 data were used as valid data and the rest of the collected data (3000) were used for testing. The training process was realized on the Anaconda platform with python 3.7.7, pytorch 1.5.0 and torchvision 0.6.0. The configuration of the computer we used is: AMD Ryzen 5 3600 (6-Core Processor, 3.6 GHz), Nvidia GeForce RTX 2060 (6GB), SSD (500GB) and DDR4 (16GB, 2666MHz). The CNN simulator takes the 5×5 matrix whose elements equal to either -1 or 1 (representing the structural configuration of a monolayer metasurface) as input, and outputs the real and the imaginary parts of the elements of the corresponding scattering matrix from 100 THz to 300 THz in the form of a linear array with 2416 elements. Thus, the loss function for the training of the CNN simulator is defined as:

$$L=\frac{\sum\limits_{i=1}^{M}\sum\limits_{j=1}^{N}\left(\left|\mathrm{Re}(S_i^{\mathrm{Pre}}(\lambda_j))-\mathrm{Re}(S_i^{\mathrm{Real}}(\lambda_j))\right|+\left|\mathrm{Im}(S_i^{\mathrm{Pre}}(\lambda_j))-\mathrm{Im}(S_i^{\mathrm{Real}}(\lambda_j))\right|\right)}{2\times M\times N}. \tag{S16}$$
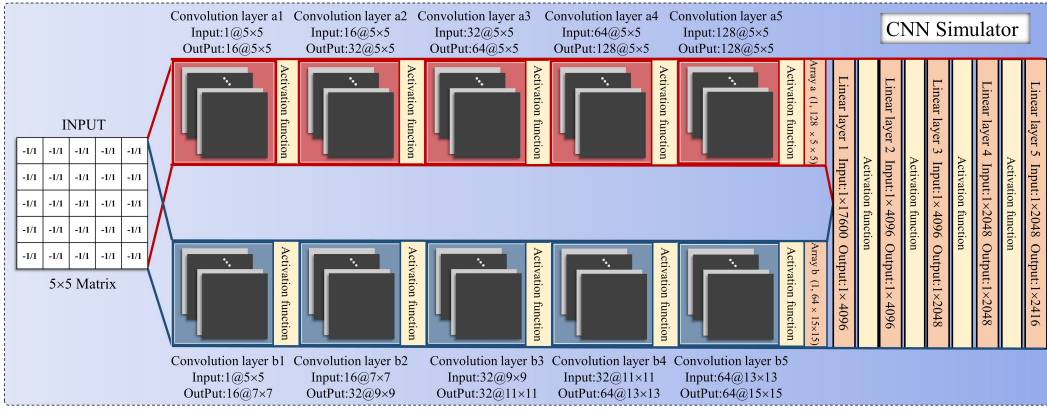
FIG. S3. Architecture of the CNN simulator. The kernel size, stride lengths and padding for convolution layer a1 to a5 equals to 3, 1, 1 respectively, while those for convolution layer b1 to b5 equals to 1, 1, 1.

Hyperparameters of the training of the CNN simulator	
Optimizer	Adam(0.9,0.99)
Batch size	200
Learning rate	0.0003
Activation function	Relu
weight decay	0.00007
Iterations	3000000

TABLE S1. Hyperparameters for the training of the CNN simulator

where M and N representing the half of the total number of the elements in the scattering matrix and the total number of the frequency points are equal to 8 and 151, respectively. $S_i^{\mathrm{Pre}}(\lambda_j)$ and $S_i^{\mathrm{Real}}(\lambda_j)$ represent the predicted and the simulated value of the i element of the scattering matrix at the frequency point λ_j. The hyperparameters for the training of the CNN simulator are shown in Table S1, which were fixed after various tests with the same training data set. The trained CNN simulator has been tested by using the test data set containing 3000 data, result indicates that the scattering matrices of 95.8% test data can be well predicted while the corresponding values of the loss function are less than 0.05.

IV. DETAILS OF THE EVOLUTION STRATEGY

The flowchart of the evolution algorithm is shown in Figure S4(a). For the design of a few-layer metasurface in which the number of layers is equal to N, N species with population size equal to S are firstly generated. Each species is associated with the structural configuration of one layer of the few-layer design, for example, species 1 is associated with the structural configuration of layer 1 (Figure S1(d)).The individuals in every species are 5×5 matrices whose elements equal to either 1 or -1. In our algorithm, the population size S is chosen as 100. A spacing list with length N representing the distance between the layers in the few-layer metasurface is initially defined. Owing to the physical mechanism of the multiple wave interference effect, the optical responses of few-layer metasurfaces are periodical changed with the variation of the distances between the layers. In the design process of few-layer metasurfaces, the distances between the layers are always less than the half of the operating wavelength. In our algorithm, the initial value of the elements in the spacing list are chosen as 250 nm with the variation range from 120 nm to 700 nm. We employ the individuals with same index in each species to constitute a few-layer metasurface marked with the same index, for example, the few-layer metasurface with the index equal 1 is composed of S1-1, S2-1, SN-1. The scattering matrices of individuals in each species are predicted by the well-trained CNN simulator. By combining the list of the few-layer metasurfaces and the spacing list, the scattering matrix of each generated few-layer metasurface can be obtained based on the matrix theory of multilayer optics. A fitness function is defined to quantitively calculated the difference between the objective scattering matrix and the predictive ones:
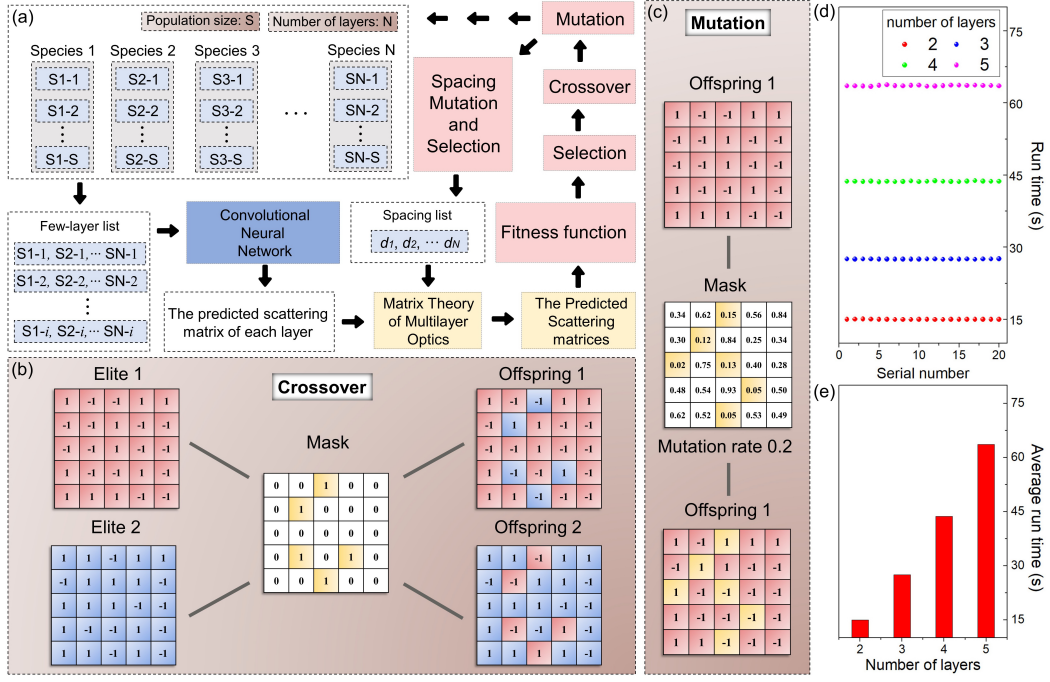
FIG. S4. Illustrating of the evolution strategy. (a) Flowchart of the evolution algorithm. (b) Crossover strategy. (c) Mutation strategy.(d) Time cost for the inverse design of few-layer metasurfaces with different number of layers in multiple runs. (e) Average time cost for the inverse design of few-layer metasurfaces with different number of layers.

$$Score = \frac{\sum\limits_{i=1}^{M} \sum\limits_{j=1}^{N} \left(\left| \text{Re}(S_i^{\text{Pre}}(\lambda_j)) - \text{Re}(S_i^{\text{Obj}}(\lambda_j)) \right| + \left| \text{Im}(S_i^{\text{Pre}}(\lambda_j)) - \text{Im}(S_i^{\text{Obj}}(\lambda_j)) \right| \right)}{2 \times M \times N} \ , \tag{S17}$$

where M and N represent the total number of the considered elements in the scattering matrix and the total number of the frequency points, respectively. $S_i^{\text{Pre}}(\lambda_j)$ and $S_i^{\text{Obj}}(\lambda_j)$ represent the predictive and the objective value of the i element of the scattering matrix at the frequency point λ_j. After the evaluation of the fitness score, the individuals in each species are ordered according to the corresponding scores from small to large. In the selection process, the 30 individuals with best scores (smaller values) are selected in each species as elites. The selected elites are involved as offspring in the new species for the next loop. In the crossover process, another seventy offspring are generated in each new species for the next loop. The crossover strategy is shown in Figure S4(b). For every crossover process, a 5×5 matrix whose elements equal either 1 or 0 is randomly generated. Then, the indexes of the elements whose value equal to 1 are recorded. Two elites are randomly selected and their elements whose indexes are equal to the recorded ones are exchanged to generate two offspring. The new species for the next loop are formed after the mutation process. As shown in Figure S4(c), for a generated offspring, a 5×5 matrix is randomly generated; The values of the elements in the generated matrix follow uniform distribution with the range of values from 0 to 1. The indexes of the elements of the generated matrix whose value are low than the mutation rate (defined as 0.2 in our algorithm) are then recoded. Then, the elements of the generated offspring whose indexes are equal to the recorded ones are changed from 1 to -1 (or -1 to 1). Before the next loop, the elements in the spacing list are further adjusted. The elements in the spacing list are firstly normalized as:

$$d_i^{\text{Norm.}} = \frac{d_i - d_{\min}}{d_{\max} - d_{\min}} \ , \tag{S18}$$

where $d_{\max}$ and $d_{\min}$ representing the lower limit and the upper limit of the value of the elements in the spacing list are equal to 120 and 700, respectively. Then, one hundred lists with N elements are randomly generated; the values of the elements in the generated lists follow gaussian distribution with the standard deviation equal 5. A species of the spacing list is formed by adding the normalized spacing list and the one hundred generated lists. Then the values of the elements in the individuals of the specie of the spacing list are recovered to their real values based on Equation

S18. The individuals in the specie of the spacing list are evaluated with the new species of the structures (same index) by using the fitness function. The individual with best score (minimum value) in the specie of the spacing list is chosen as the new spacing list in the next loop. The total number of loops is 60. Then, the N 5×5 matrices (with the best score) representing the structural configurations of each individual layer and the spacing list representing the distance between the layers are outputted. Since N species are needed for the inverse design of few-layer metasurfaces with N layers, the time cost will increase as the number of layers grows, as shown in Figure S4(d), (e). The results indicate that the time cost for the inverse design of the few-layer metasurfaces will be less than one minute when the number of layers of few-layer metasurfaces is less than five. Therefore, the proposed inverse design method is much faster than the design and optimization method based on an iterative numerical simulation process of trial and error, for which the expended time depends on personal experience, which always take several hours, days or weeks.

V. DATA SUPPORTING THE DISCUSSION OF THE ADVANTAGES AND LIMITATIONS OF THE PROPOSED ALGORITHM

The implementation of the inverse design of few-layer metasurfaces by the proposed algorithm is based on the evolution algorithm, which can tackle the one-to-many mapping problem and the existence or nonexistence problem. With appropriate mutation and crossover strategy, the evolution algorithm tends to find a few-layer metasurface whose optical response can meet or close to the on-demand optical functionality. On the one hand, the proposed algorithm can find the few-layer metasurface with best score (a minimum value of fitness function) in every run. Even if there is no such a few-layer metasurface whose optical response can fully satisfy the required optical functionality, the few-layer metasurface whose optical response is close to the on-demand functionality can also be obtained. On the other hand, since the initialization and evolution process are random, the inversely designed few-layer metasurfaces by multiple runs will be different for a required optical functionality. However, the optical responses of the few-layer metasurfaces obtained by multiple runs are similar, which are close to the required optical functionality. As an example, Figure S5 shows three bilayer metasurfaces inversely designed by three runs, for which the required optical functionality is shown in Figure 3a. It is obvious that the structural configurations of these three designs are different and they are also different to the one in Figure 3b. However, the optical functionalities are similar and close to the desired functionality.

Compared with previous inverse design approaches in which the targets are always focused on one or two fixed optical characteristics (such as transmission spectrum, reflection spectrum, the phase and amplitude of transmission wave, and so on), the proposed algorithm can predict the entire scattering matrix of a few-layer metasurface in a broad
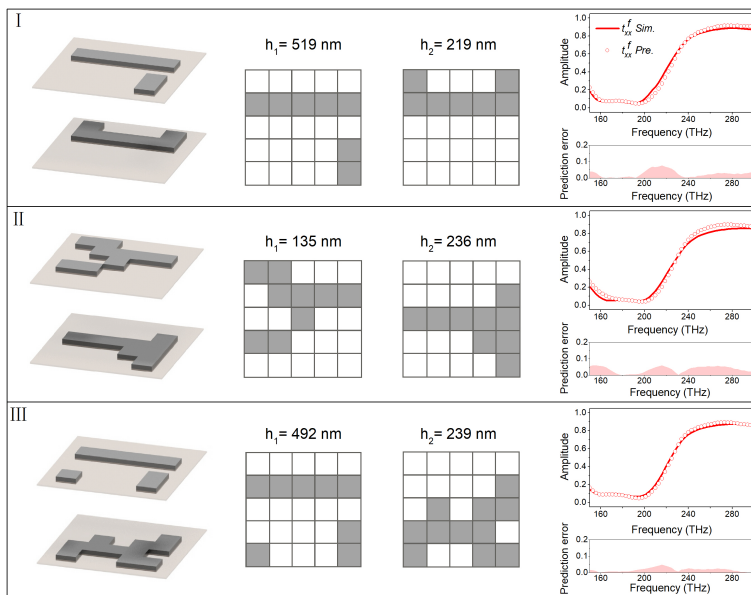

FIG. S5. Inverse design of the bilayer metasurfaces as optical filters based on the proposed EV-CNN-MT deep-learning algorithm. The structural configurations, the predicted and the simulated results of the optical responses of the three designed bilayer metasurfaces and the corresponding prediction errors.
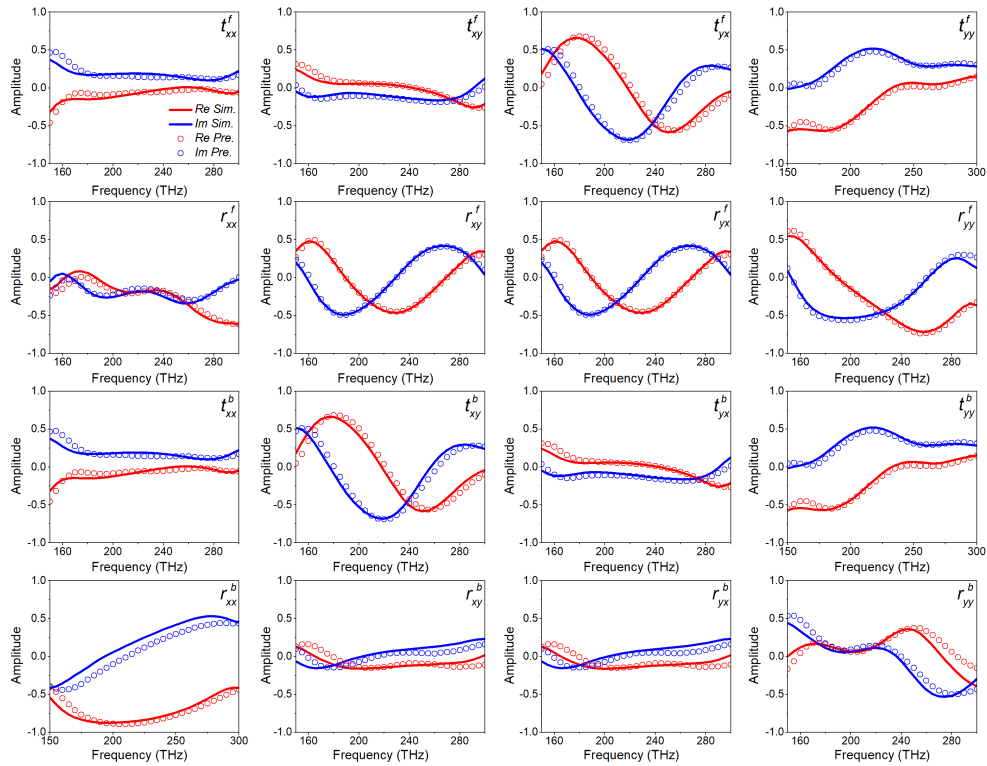
FIG. S6. The simulated and the predicted results of the real and the imaginary parts of the coefficients of the scattering matrix of the designed bilayer metasurfaces in Figure 3j.

bandwidth within an acceptable prediction error range. An example is presented in Figure S6. It means that the proposed algorithm is universal applicable, which can be used to realize the inverse design of few-layer metasurfaces with different optical functionalities and multiple functionalities, as shown in Figure 3.

Even the CNN simulator is well trained, the prediction accuracy of the CNN simulator needs to be further improved. Since the scattering matrices of the few-layer metasurfaces are calculated by the predicted scattering matrices of each layer, the prediction errors of the scattering matrices of the monolayers will significantly affect the prediction accuracy of the scattering matrices of the few-layer metasurfaces, especially when the amplitude of the element of the scattering matrices of the monolayers tend to 1. For example, there is a visible difference between the predicted and the simulated t_{yy}^{f} from 150 THz to 180 THz in Figure 3o, which is attributed to the prediction errors of t_{yy}^{f} of the two monolayers, as shown in Figure S7 and Figure S8.
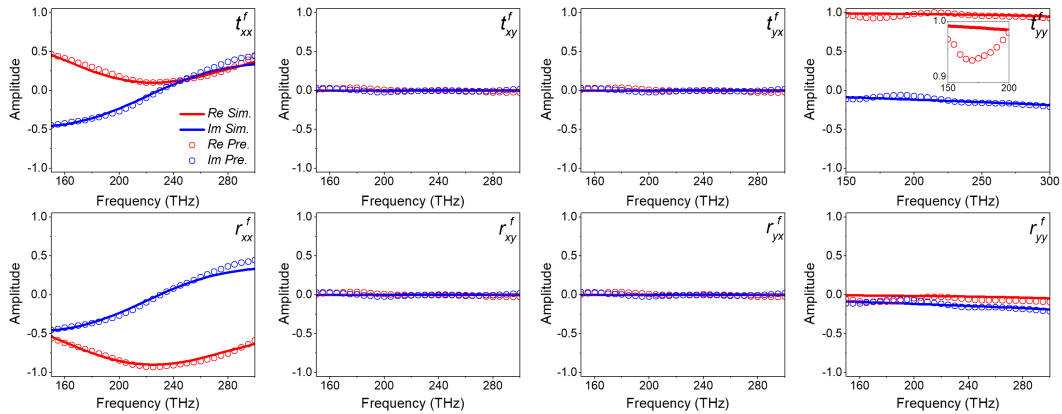

FIG. S7. The simulated and the predicted results of the real and the imaginary parts of the coefficients of the scattering matrix of the top layer of the designed bilayer metasurfaces in Figure 3n.
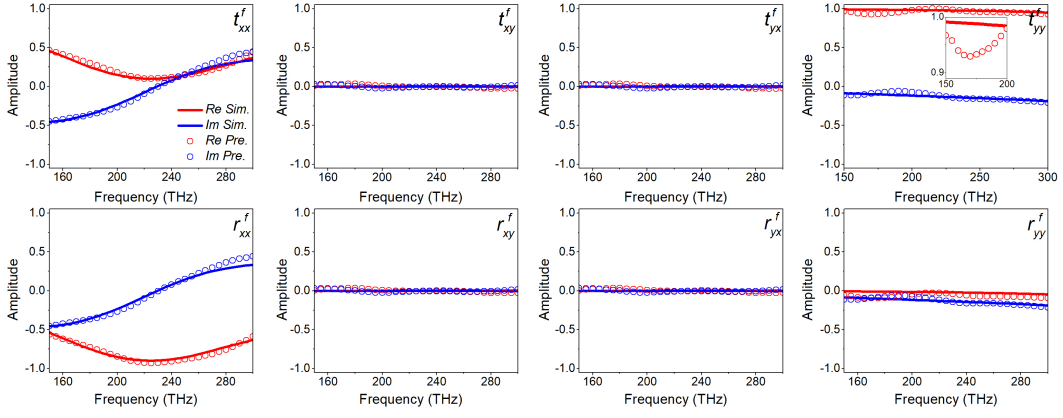
FIG. S8. The simulated and the predicted results of the real and the imaginary parts of the coefficients of the scattering matrix of the bottom layer of the designed bilayer metasurfaces in Figure 3n.

VI. STRUCTURAL CONFIGURATIONS OF THE DESIGNED METASURFACES

The designed few-layer metasurfaces can be fully represented by the aluminum nanostructures in each layer and the distances between each adjacent layer, as shown in Figure S9 to Figure S11. In each layer of the designed few-layer metasurfaces, the periods of a unit cell in both the x and y directions are 450 nm. As we mentioned above, the periodic planar aluminum nanostructures in each layer consist of several aluminum cuboids in which width $w = 70$ nm and thickness $t = 30$ nm. Every planar aluminum nanostructure is related to a 5×5 matrix in which the elements are equal to either 0 or 1. When the element of the matrix equals 1, an aluminum cuboid is built in the corresponding place. Otherwise, no aluminum cuboid is built.
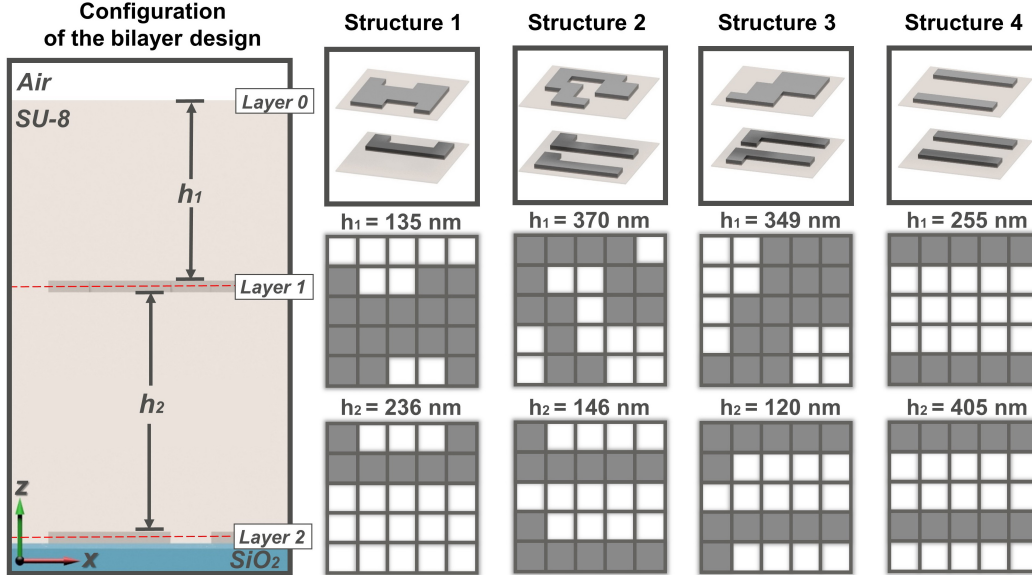

FIG. S9. Illustrating of the bilayer design and the structural configurations of the designed metasurfaces in Figure 3. The designed metasurfaces are fully described by the planar aluminum structures in each layer and the distance between the adjacent layers.
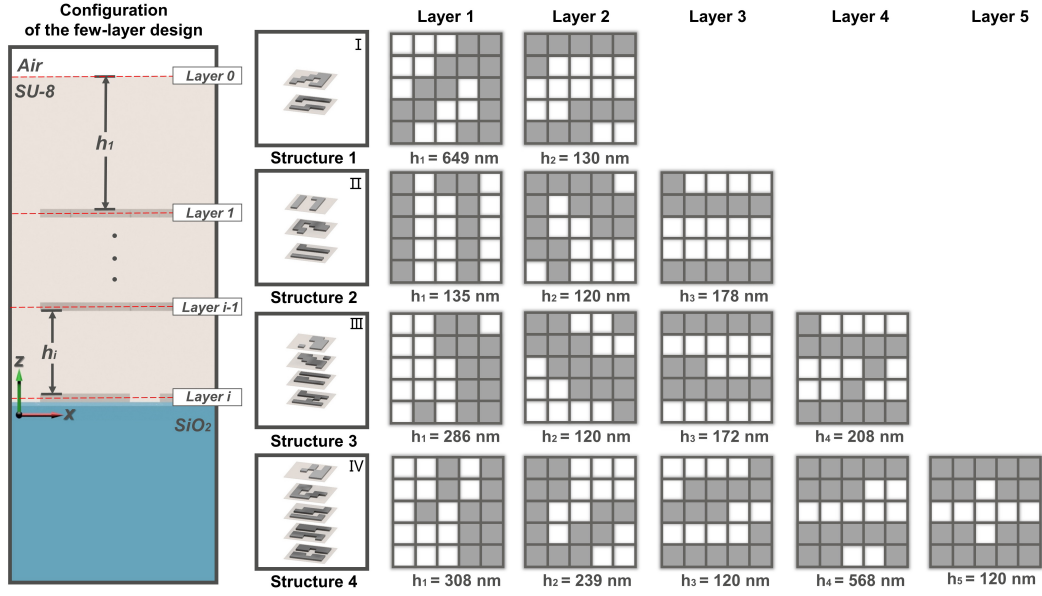
FIG. S10. Illustrating of the few-layer design with i layers and the structural configurations of the designed metasurfaces in Figure 4.
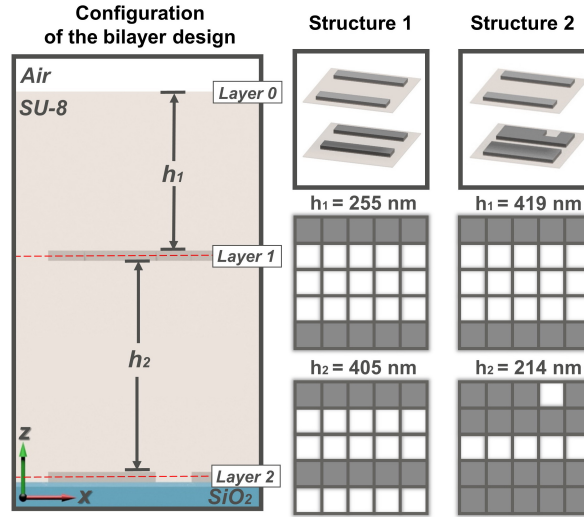

FIG. S11. Illustrating of the bilayer design and the structural configurations of the designed metasurfaces in Figure 5.

VII. SAMPLE FABRICATION AND MEASUREMENT METHODS

Sample fabrication : The designed aluminum few-layer metasurfaces were fabricated by electron-beam lithography (EBL), and aluminum (Al) lift-off process. A 200 nm thick positive electron-beam resist of ZEP520A was initially spin-coated onto a microscope slide glass, and then the nanorod pattern was exposed using an EBL system (RAITH 150) at 30 keV. After the exposure, the sample was developed in n-amyl acetate for 60s, rinsed with isopropanol, and then blown dry using pure nitrogen. A 30 nm thick Al film was subsequently deposited by using an electron-beam evaporator (Temescal BJD-2000). After the resist was removed by means of a ZEP remover (ZDMAC), the first layer of the Al nanostructures was created. A layer of the SU-8 polymer with the designed thickness was then spun coated onto the sample and UV-cured. The Al nanostructures in other layers and other layers of the SU-8 polymer were prepared by repeating the above-mentioned processes. Finally, a SU-8 polymer with designed thickness was spun coated on top of the sample and UV-cured. Each of the completed few-layer metasurfaces occupy a footprint less

than 100 μm$\times$100 μm. In addition, the misalignment between the two-layer nanorods is less than 100 nm.

Experimental measurement : The optical spectra were measured by using a Fourier transform infrared spectrometer (VERTEX 70, Bruker Optics, Ettlingen, Germany) coupled to an IR microscope (Hyperion 2000, Bruker Optics, Ettlingen, Germany). The spectral data were acquired with the OPUS 6.0 software. Air was used as the reference for measuring the transmittance.

* hcheng@nankai.edu.cn

† schen@nankai.edu.cn

[1] N. K. Grady, J. E. Heyes, D. R. Chowdhury, Y. Zeng, M. T. Reiten, A. K. Azad, A. J. Taylor, D. A. R. Dalvit, and H. T. Chen, Terahertz metamaterials for linear polarization conversion and anomalous refraction, Science **340**, 1304-1307(2013).

[2] C. Menzel, C. Rockstuhl, and F. Lederer, Advanced Jones calculus for the classification of periodic metamaterials, Phys. Rev. A **82**, 053811(2010).

[3] E. D. Palik, Handbook of Optical Constants of Solids (Academic Press, New York, 1998).